Platinum-Grafted Twenty-Five Atom Gold Nanoclusters for Robust Hydrogen Evolution

*Paloli Mymoona, Jose V. Rival, Nonappa, Edakkattuparambil Sidharth Shibu, * Chinnaiah Jeyabharathi **

C.J. dedicates this article to Dr. Kanala Lakshminarasimha Phani, Chief Scientist (retired), for his mentorship

P. Mymoona, Dr. C. Jeyabharathi (Senior Scientist)
Council of Scientific and Industrial Research (CSIR)-Central Electrochemical Research Institute (CECRI), Karaikudi-630003, Tamil Nadu, India.
Academy of Scientific and Innovative Research (AcSIR), Ghaziabad-201002, India.
Email: bharathchem@gmail.com or cjeyabharathi@cecri.res.in

J. V. Rival, Dr. E. S. Shibu (Assistant Professor)
Smart Materials Lab, Department of Nanoscience and Technology (DNST), University of Calicut (UOC), Malappuram-673635, Kerala, India.
Email: shibuchem@gmail.com or shibues@uoc.ac.in
orcid.org/0000-0003-3057-4198

Dr. Nonappa
Associate Professor
Faculty of Engineering and Natural Sciences, Tampere University, P.O. Box 541, FI-33101 Tampere, Finland.

Keywords: Catalysis. electrochemical activation. hydrogen evolution reaction. precision nanoclusters. supramolecular assembly.

We demonstrate a robust hydrogen evolution from $Au_{25}(PET)_{18}]^{-}$ nanoclusters grafted with minimal platinum atoms. The fabrication involves an electrochemical activation of nanoclusters by partial removal of thiols, without affecting the metallic core, which exposes Au-sites adsorbed with hydrogen and enables an electroless grafting of platinum. The exposed

Au-sites feature the (111)-facet of the *fcc*-Au_{25} nanoclusters as assessed through lead underpotential deposition. The electrochemically activated nanoclusters (without Pt loading) show better electrocatalytic reactivity towards hydrogen evolution reaction than the pristine nanoclusters in an acidic medium. The platinum-grafted nanocluster outperformed with a lower overpotential of 0.117 V_{RHE} compared to electrochemically activated nanoclusters (0.353 V_{RHE}) at 10 mA cm^{-2} and is comparable with commercial Pt/C. The electrochemically activated nanoclusters show better reactivity at higher current density owing to the ease of hydrogen release from the active sites. The modified nanoclusters show unique supramolecular self-assembly characteristics as observed in electron microscopy and tomography due to the possible metallophilic interactions. These results suggest that the post-surface modification of nanoclusters will be an ideal tool to address the sustainable production of green hydrogen.

1. Introduction

The sustainable solution to the energy and environmental crisis relies on new technologies based on hydrogen,[1] which has been explored as a renewable energy carrier with high energy density. In particular, electrolysis of water, which is abundant and renewable, is considered a means to produce green hydrogen.[2] For achieving high energy efficiency, inexpensive and active electrocatalysts are needed. Platinum (Pt) is the most promising hydrogen evolution reaction (HER) catalyst that exhibits lower overpotentials.[3] However, Pt is the least abundant and expensive metal, hampering commercial-scale electrolyzer development.[4] Recently, nanoparticles (NPs) have been studied for HER due to their size, shape, and geometry-dependent catalytic properties.[3b] However, conventional NPs display polydispersity, batch-to-batch variation, and aggregation tendency during the catalytic process. Despite tremendous efforts, it still remains challenging to develop highly active HER catalysts based on non-Pt sources for acidic medium.[5] Low-loading Pt-based electrocatalysts are one of the ways to reduce the cost without compromising the reactivity.[6] Alloying Pt with other metals such as Ru, Mo, Ni, and Co reduces the utilization of Pt and is shown to improve efficiency.[3b,7]

However, the cost reduction is not appreciable. In this context, thiolate-protected atomically precise noble metal nanoclusters (NCs) display well-defined atomic and electronic structures that hold promising applications in catalysis/electrocatalysis,[8] energy conversion,[9] photovoltaics,[10] and sensing[11] owing to their small size, quantum confinement, better chemical/photostability, diverse surface functionalities, and unique optoelectronic properties.[8a,12] Among several thiol-protected NCs reported, well-studied examples include $[Au_{25}(SR)_{18}]$,[13] $[Au_{38}(SR)_{24}]$,[14] $[Au_{102}(SR)_{44}]$,[15] and so on. The electrocatalytic activity of gold (Au) NCs could be considerably enhanced through their atomic-level modifications like core size,[16] doping/alloying,[17] charge,[9] types of ligands,[18] and ligand "On and Off" effects.[16e]

Brust and Gordillo showed that reversible hydrogen adsorption and oxidation are possible on the thiolate-protected Au NCs.[19] In general, atomic NCs are known to enhance the electrocatalytic activity of surface-sensitive reactions.[20] For HER the pristine Au NCs possessed poor electrocatalytic performances. However, the reactivity enhancement has been accomplished through various approaches, including (i) doping with Pt, Pd, Cu, Cd, and Ag,[17,21] and (ii) compositing with chalcogenides, etc.[16e,22] These developments demonstrate promising outcomes for electrocatalytic water-splitting applications in both aqueous and non-aqueous media. However, in NCs, strong chemical adsorption of thiolate ligands on the metal surfaces would passivate the active sites and reduce the catalytic activity. Dethiolation-based activation of the NC surface by an electrochemical method, enhanced the reactivity of carbon dioxide reduction reactions (CO_2RR),[16d] whereas the complete removal of ligands would promote aggregation and coalescence leading to the growth of NCs into NPs that cost the catalytic activity. Instead, systematic adjustment of core composition and ligands is suitable to tailor the structure and electronic properties of NCs and enable a new category of nanomaterials in electrocatalysis.

Herein, we report the electrochemical (EC) activation of 2-phenylethane thiol (PET)-tethered Au_{25} NCs as a catalyst for HER. Moreover, the EC-activated NCs have been modified with Pt atoms through the electroless strategy based on the intermediates generated during EC-activation. The pristine Au_{25} NCs, EC-activated Au_{25} NCs, and Pt-decorated Au_{25} NCs have been studied in detail using various electrochemical, spectroscopic, and microscopic techniques. The EC-activated Au_{25} NCs behaved better than the pristine NCs, and Pt-decorated NCs exhibited improved HER activity very close to the commercial Pt/C. This enhancement was evident with an overpotential of 0.117 V vs RHE, at a current density of 10 mA cm^{-2}. These Pt-decorated Au_{25} NCs also exhibited an exchange current density of 0.43 mA cm^{-2} and a Tafel slope of 86 mV dec^{-1}, despite the utilization of an exceptionally small amount of Pt.

2. Results and Discussion

2.1. Synthesis and characterization of $[Au_{25}(PET)_{18}]^{-}$ NCs

Pristine $[Au_{25}(PET)_{18}]^{-}$ NCs (Au_{25} NCs) were synthesized and purified using the modified Brust-Schiffrin method (**Scheme S1**).[23] The Ultraviolet-Visible (UV-Vis) absorption spectrum of purified Au_{25} NCs dispersed in dichloromethane (DCM) displayed a characteristic HOMO-LUMO peak at *ca*. 680 nm and HOMO-sp and d-sp transitions at *ca.* 450 nm and *ca.* 400 nm, respectively, suggesting the presence of monodispersed NCs (**Figure 1**b). The High Resolution-Transmission Electron Microscopic (HR-TEM) analysis of the NCs shows a uniform size distribution (1.5 ± 0.5 nm; **Figure 1**c). The Electrospray Ionization-Mass Spectrometry (ESI-MS) showed a molecular ion peak of *ca.* m/z 7391, comparable with the reported spectrum of Au_{25} NCs with matching experimental and isotopic distribution (**Figure 1**d). The Au_{25} NC is composed of an Au_{13} icosahedron core that is protected by six pairs of $Au_2(PET)_3$ staple motifs (**Figure 1**a). These six $Au_2(PET)_3$ staple motifs are arranged as V-shaped semi-rings. The icosahedron has eight uncapped Au_3 faces and additional 12 faces are capped with the staple motifs on the icosahedral Au_{13} core. The energy-minimized structure of

Au_{25} NC optimized using the density functional theory (DFT) is shown in **Figure 1**a. The X-ray Photoelectron Spectrum (XPS) analysis revealed the binding energy (BE) values of Au $4f_{7/2}$ 84.38 eV and Au $4f_{5/2}$ 88.03 eV (**Figure 1**e). The BE of sulfur $2p_{3/2}$ and $2p_{1/2}$ states appear 162.61 eV and 163.80 eV, which is in agreement with Au-S bonding, (**Figure 1**f).

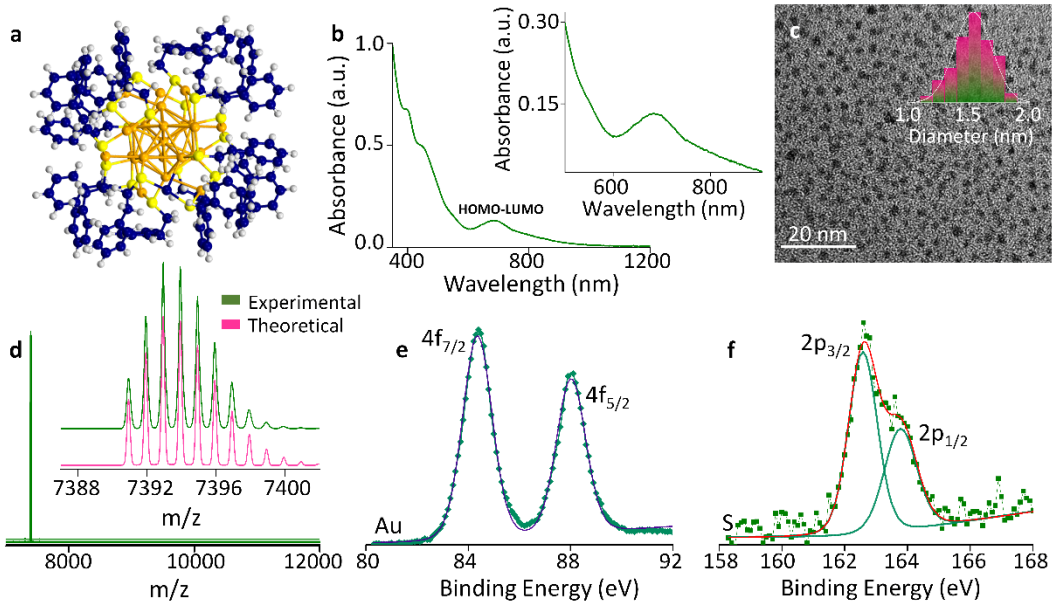

Figure 1. Synthesis and characterization of Au_{25} NCs. (a) Energy-minimized structure of Au_{25} NCs. (b) UV-Vis absorption spectrum of Au_{25} NCs. The inset shows the HOMO-LUMO transition. (c) The HR-TEM image of Au_{25} NCs with size distribution. (d) ESI-MS of the Au_{25} NCs with experimental (green) and theoretical (pink) isotopic patterns highlighted. (e, f) XPS spectra of Au 4f and S 2p of Au_{25} NCs.

2. 2. Electrochemical activation of Au_{25} NCs

The cathodic treatment in polar/non-polar electrolytes is one of the interesting activation strategies, e.g. large particles can be corroded cathodically and redeposited as smaller particles. This pushed the limitation of the electrochemical methods to control the size of the deposited particles. Cherevko *et al*. used cathodization for the surface modification of polycrystalline Au with Pt, where Au-H and/or Au NCs were formed on the surface and were utilized for Pt deposition.[24] Two possible scenarios for the electroless-grafting on polycrystalline Au was

attributed: (a) reduction of Pt ions by Au-H; (b) galvanic exchange of Pt ($E°_{\frac{PtCl_6^{2-}}{Pt_{Poly}}}$ = 0.742 V_{RHE})[25] (hereafter, all potentials are reported vs. RHE unless noted otherwise) with Au NCs formed at high cathodic potentials. The galvanic exchange is feasible only if the standard potential of the surface asperities/NCs is altered.[26] Here, the standard reduction potential of gold adatom is more negative ($E°_{\frac{AuCl_4^-}{Au_{adatom}}}$ = -0.135 V) than that of the polycrystalline Au ($E°_{\frac{AuCl_4^-}{Au_{poly}}}$ = 1.01 V). In our case, contrarily, cathodization of thiolated Au_{25} NCs was performed for a short period of time. This led to the formation of activated NCs deprived of few ligands (partial de-thiolation) due to the reductive desorption of thiols exposing free Au-sites. On those free-Au sites, Au-H formation is a prominent process at such negative potentials in aqueous solutions. Subsequently, the electroless-grafting of Pt over the activated Au_{25} NCs was achieved by immersing it in chloroplatinic acid (**Figure 2**). Because of the adsorbed hydrogen, electroless-grafting of Pt might take place rather than the galvanic replacement of Pt with Au atoms as discussed in the upcoming sections. Further, pristine Au_{25} NCs, EC-activated [$Au_{25}(PET)_m$] NCs (denoted as EC-Au_{25} NCs; m - number of ligands after EC-activation), and [Pt_n-$Au_{25}(PET)_m$] NCs (denoted as Pt-Au_{25} NCs; n - number Pt atoms) were used for electrochemical characterization and reactivity studies.

The extent of exposed Au sites in Au_{25} NCs was assessed by measuring the electrochemically active surface areas (ECSA) in deaerated 0.1 M H_2SO_4 from -0.25 to 1.45 V at 50 mV s^{-1} (**Figure 3**a, **Figure S1** for results in oxygen saturated electrolyte). The voltammetric response of Au_{25} NCs displayed only the capacitive features, indicating that the surface is passivated with thiol ligands. The voltammogram of EC-Au_{25} NCs showed the onset of Au oxidation at *ca.* 1.0 V vs Ag/AgCl with a peak potential of *ca*.1.2 V vs Ag/AgCl and a cathodic gold oxide reduction at *ca*. 0.9 V vs Ag/AgCl, confirming the exposition of Au sites on the surface of NCs. Upon the electroless-grafting of Pt atoms on EC-Au_{25} NCs, the onset potential of surface

oxidation is shifted by 0.25 V vs Ag/AgCl to less-positive potentials since Pt is oxidized prior to Au. Also, the anodic Au oxidation peak is obscured and the intensity of the gold oxide reduction peak at ~ 0.9 V vs Ag/AgCl is suppressed, which is due to the Pt-decoration on exposed Au atoms. In addition, a cathodic peak was observed at 0.4 V vs Ag/AgCl corresponding to platinum oxide reduction followed by underpotential deposition (UPD) of hydrogen and subsequent hydrogen evolution. All these signatures ensure that the Pt is decorated over the EC-Au_{25} NCs. The H-UPD was also oxidized in the positive-going potential sweep, which was utilized to evaluate the ECSA. Moreover, the surface-sensitive Pb-UPD measurement was also employed to assess the extent of ligand removal from the pristine Au_{25} NCs by determining ECSA from the Pb-UPD charge[27]. **Figure 3**b shows the Pb-UPD cyclic voltammogram of Au_{25}, and EC-Au_{25} NCs measured between the potential of -0.4 to 0.3 V vs Ag/AgCl with a scan rate of 20 mV s^{-1}. The pristine Au_{25} NCs showed no peaks in the Pb-UPD region, which implied that their Au sites are passivated. A weak Pb-UPD signature started appearing at -0.26 V vs Ag/AgCl after EC-activation. This indicates the removal of a few of the ligands of Au_{25} NCs exposing free Au sites. This Pb-UPD signal may be attributed to the defective Au sites since the potential does not correspond to any identifiable crystallographic orientation. Cycling of the EC-Au_{25} NCs in the Pb-UPD potential window shows the evolution of different identifiable Pb-UPD peaks attributed to terraces and steps of Au, indicating the possible electrochemical ripening of NCs. The stripping peaks at *ca.* -0.27 and *ca.* 0.03 V vs Ag/AgCl are attributed to Au(110) terrace and the peak at *ca.* -0.19 V vs Ag/AgCl is attributed to Au(111) terrace (**Figure S2**). The observation of the characteristic peaks suggests the possible exposure of few-atom width steps and terraces upon electrochemical ripening. The evolution of the Pb-UPD signal is similar to the removal of a self-assembled thiol monolayer from the Au surface by hydroxyl radicals[28]. The UV-Vis absorption spectra of EC-Au_{25} NCs after Pb-UPD cycling show unaltered absorption spectra after cycling in the UPD potential

window. This indicates the refinement of exposed Au sites retaining the core structure (**Figure 3**d). It is well known that Au_{25} NCs possess the *fcc* lattice structure[12a] and thus the exposition of the surface sites would possess the characteristics of Au(111) and Au(110), which are highly stable low-index planes. To the best of our knowledge, this is the first observation of detecting the *fcc* structure of Au_{25} NCs using Pb-UPD. In addition, from the charge of gold oxide reduction, the ECSA of EC-Au_{25} NCs was measured by considering the charge related to gold oxide reduction as 390 µC cm^{-2}. The results show that EC-Au_{25} NCs have an ECSA of 0.0113 cm^2, which is similar to the ECSA calculated from the Pb-UPD stripping peak (0.0114 cm^2). The ECSA of Pt-Au_{25} NCs was calculated by integrating the charge associated with H-UPD desorption on the Pt is 0.0145 cm^2 (**Figure S3**a and b, **Text S2**). Similarly, the ECSA of the commercial Pt/C catalysts was calculated (**Figure S4**) and is found to be 0.1747 cm^2. The difference in ECSA is due to the ultra-low loading of Pt on Au_{25} NCs. The loading of Pt achieved through the electroless decoration process was determined to be 0.8 µg cm^{-2} from the hydrogen stripping charge (30.45 µC). It's worth noting that this loading is 7 times lower when compared to the Pt/C (**Text S3**). The ECSA values are presented as a histogram (**Figure 3**c) and are tabulated in **Table S1**. The method of calculation of ECSA is explained in the **Text S1**.

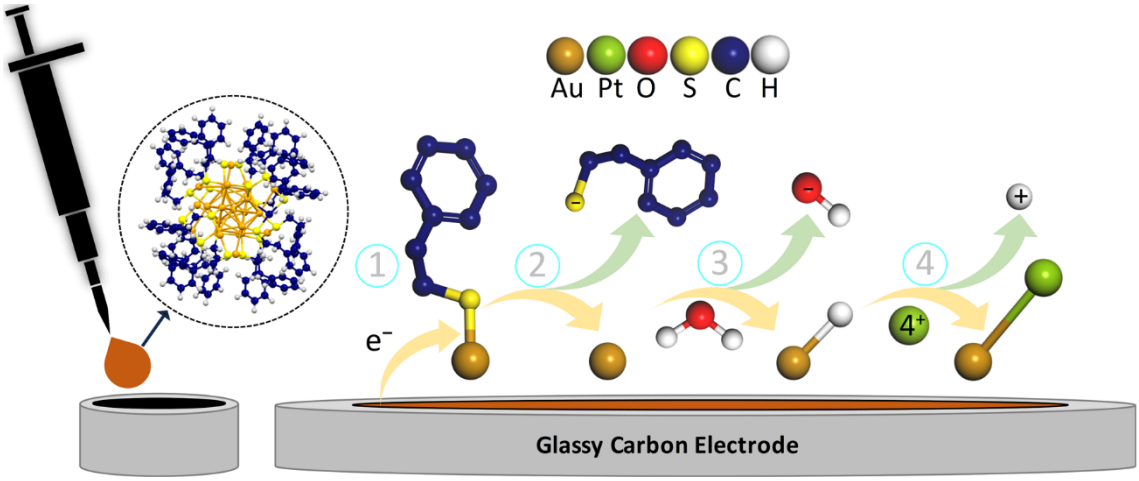

Figure 2. Schematic representation of EC-activation and subsequent Pt-grafting.

The integrity of the structure of pristine, EC-Au_{25}, and Pt-Au_{25} NCs was studied by comparing their UV-Vis absorption spectra (**Figure 4**a). The unchangeable HOMO-LUMO transition (*ca*. 680 nm) in EC-Au_{25} NCs (blue line) and Pt-Au_{25} (pink line) confirms the stability of core Au_{25} NCs towards EC-activation and subsequent electroless grafting of Pt. Furthermore, the ESI-MS pattern of Au_{25} NCs shows an intense peak at m/z 7391 (**Figure 4**b). However, after EC-activation, the pattern was shifted to a lower mass, which might indicate the thiol removal. After Pt-decoration, the pattern was still in the lower mass region, but with minor changes in the position. Here, counting the number of thiols removed and Pt atoms decorated is challenging due to one-second EC-activation, very small mass difference (1.882 amu) between Au (196.966 amu) and Pt (195.084 amu), and limited resolution of the mass-spectra. A similar mass spectrum of single Pt-doped Au_{25} thiolated NCs was observed by Jin *et al*.[29] To quantify the amount of thiol removed during EC-activation, we have recorded Gas Chromatography-Mass Spectrometry (GC-MS) of EC-Au_{25} NCs. **Figure S5**a shows the GC-MS experimental data of four standard PET solutions with known concentrations and an unknown solution with and without the addition of a standard (1000 ng mL^{-1}). The removed thiols are detected matching with the standard data with a retention time of ca. 6.86 (**Figure S5**b). The GC-MS analysis confirms the removal of thiol from NCs during the EC-activation, and the amount of thiol removed from 4 µg of NCs is calculated to be *ca*. 0.0625 µg (1.5 % of total NC content) (**Figure S5**c). The UV-Vis spectra, ESI-MS, and GC-MS results suggest that the core-NC structure was not affected by the EC-activation. Hence, the galvanic replacement of Au with Pt is not possible on the EC-Au_{25} NCs, and the only possibility for Pt-decoration is through adsorbed hydrogen formed at -4 V. The standard potential of H-Au_{25} with the redox state of -1/0, is -0.70 V, which is more negative than the standard potential of gold adatom, -0.135 V and thus, thermodynamically, the Pt-decoration through the electroless-grafting involving

adsorbed hydrogen is favored.[30] The utilization of adsorbed hydrogen for Pt-decoration is a self-terminating process without allowing further growth.

To gain insights into the surface states of pristine Au_{25}, EC-Au_{25}, and Pt-Au_{25} NCs, XPS spectra were recorded (**Figure 4**c). In the deconvoluted spectrum of EC-Au_{25} NCs, there was a shift to the lower BE by *ca*. 0.22 eV [Au $4f_{7/2}$ 84.16 eV and Au $4f_{5/2}$ 87.85 eV] compared to that of pristine NCs [Au $4f_{7/2}$ 84.38 eV and Au $4f_{5/2}$ 88.03 eV]. This BE shift suggests that the free-Au sites are exposed after activation have a less electropositive character[31]. The deconvoluted spectrum of Pt-Au_{25} NCs exhibited similar BE values [Au $4f_{7/2}$ 84.17 eV and Au $4f_{5/2}$ 87.85 eV] of EC-Au_{25} NCs. The Pt $4f_{7/2}$ and $4f_{5/2}$ peaks were located at 72.3 eV and 75.5 eV, in the XPS spectrum of Pt-Au_{25} NCs, which is attributed to the presence of NC-bound Pt atoms exhibiting strong electropositive character (**Figure 4**d). The deconvoluted spectra of S 2p of EC-Au_{25} and Pt-Au_{25} NCs have the BE values of S $2p_{3/2}$ 162.48 eV and S $2p_{1/2}$ 163.72 eV; S $2p_{3/2}$ 162.65 eV and S $2p_{1/2}$ 163.80 eV, respectively, which is comparable to the BE values of pristine NCs (**Figure 4**e). This suggests that the chemistry of the NCs is not altered after EC-activation and Pt-decoration. Then we determined the composition of Au_{25}, EC-Au_{25}, and Pt-Au_{25} NCs by comparing the atomic percentage ratios of Au, S, and Pt using the corresponding XPS data. The Au/S ratio in the pristine Au_{25} NCs is 1.13, whereas in EC-Au_{25} NCs, it is 1.52. In the case of Pt-Au_{25} NCs, the ratio is 1.30. These findings strongly imply the removal of thiol molecules from the pristine NCs (**Table S2** and **Text S10**).

Next, the electrocatalytic HER activity of pristine Au_{25}, EC-Au_{25}, and Pt-Au_{25} NCs was compared with that of commercial Pt/C. **Figure 5**a shows the *iR*-corrected HER polarization curves of Au_{25}, EC-Au_{25}, Pt-Au_{25} NCs, and Pt/C (20 wt %) catalysts (5.7 μg cm^{-2}) with geometric surface area normalized current density. The EC-Au_{25} NCs showed higher HER activity than pristine Au_{25} NCs, whereas Pt-Au_{25} NCs outperformed, and the activity was very close to Pt/C. The HER performance in terms of overpotentials at 10 mA cm^{-2} follows the order

of Pt/C (0.099 V) > Pt-Au_{25} (0.205 V) > EC-Au_{25} (0.456 V) > Au_{25} (0.956 V). Though a limited number of Pt was loaded on the NC surface, the overpotential difference between the Pt/C and Pt-Au_{25} NCs is only 0.106 V. The overpotential of HER on Pt-Au_{25} NCs at different current densities is provided in **Figure S6**. The improved reactivity can be understood from the efficacy of Pt and the redox chemical character of Au NCs. The redox chemical characteristics of NCs might facilitate the kinetics of HER by mediating the electron transfer processes in addition to the exposition of the surface sites of Au and the decoration of Pt.[17b] Evidence for this is observed as a reduction wave with different onset potentials prior to the HER in all Au_{25} NCs (**Figure S7**). The HER overpotential at a current density of 5.0 and 10.0 mA cm^{-2} of Au_{25}, EC-Au_{25}, Pt-Au_{25} NCs, and Pt/C catalysts is compared in **Figure 5**b. Additional control experiments were carried out, to optimize the EC-activation time of Au_{25} NCs (**Figure S8**), investigate the impact of immersion time of EC-Au NCs in chloroplatinic acid (**Figure S9**), explore the influence of various counter electrodes (**Figure S10**) and working electrodes (**Figure S11**), assess the effect of electrolyte concentration (**Figure S12**), and evaluate the impact of catalyst loading (**Figure S13**).

The *iR*-corrected HER polarization curves of Pt/C, EC-$Au_{25,}$ and Pt-Au_{25} NCs normalized by ECSA are shown in **Figure 5**c. The overpotentials at a current density of 10 mA cm^{-2} followed the same order of Pt/C (0.079 V) > Pt-Au_{25} (0.117 V) > EC-Au_{25} (0.353 V), but there is a positive shift in overpotential by 0.103 V and 0.088 V for EC-$Au_{25,}$ and Pt-Au_{25} NCs, respectively. The shifts in overpotential indicate higher reactivity of NCs after the EC-activation and Pt-decoration with the least number of active sites. A comparison of the reactivity of NCs normalized to the geometrical and ECSA is shown in **Figure 5**d. To understand the inherent HER activity of EC-Au_{25} and Pt-Au_{25} NCs, Tafel slopes were calculated. The Tafel plots corresponding to polarization curves normalized with ECSA are presented in **Figure 5**e, which exhibits the Tafel slopes of 151, 86, and 37 mV dec^{-1} for EC-

Au_{25}, Pt-Au_{25} NCs, and Pt/C, respectively. The exchange current density (j_0) is one of the factors that shows the intrinsic activity at equilibrium potential. Here, j_0 values are calculated by extrapolating the Tafel lines to zero overpotential. The j_0 value of the EC-Au_{25}, Pt-Au_{25}, and Pt/C is measured to be 0.01, 0.43, and 0.18 mA cm^{-2}, respectively. The j_0 of Pt-Au_{25} NCs is found to be ~43 times higher than that of EC-Au_{25} NCs (**Figure S14**a). Notably, this value is higher than the literature value on Pt NPs.[32] Furthermore, the specific activity of Pt-Au_{25} NCs is similar (75.79 mA cm^{-2}) at the overpotential of 0.25 V and is ~ 56-fold higher than that of EC-Au_{25} NCs (1.35 mA cm^{-2}) (**Figure S14**b).

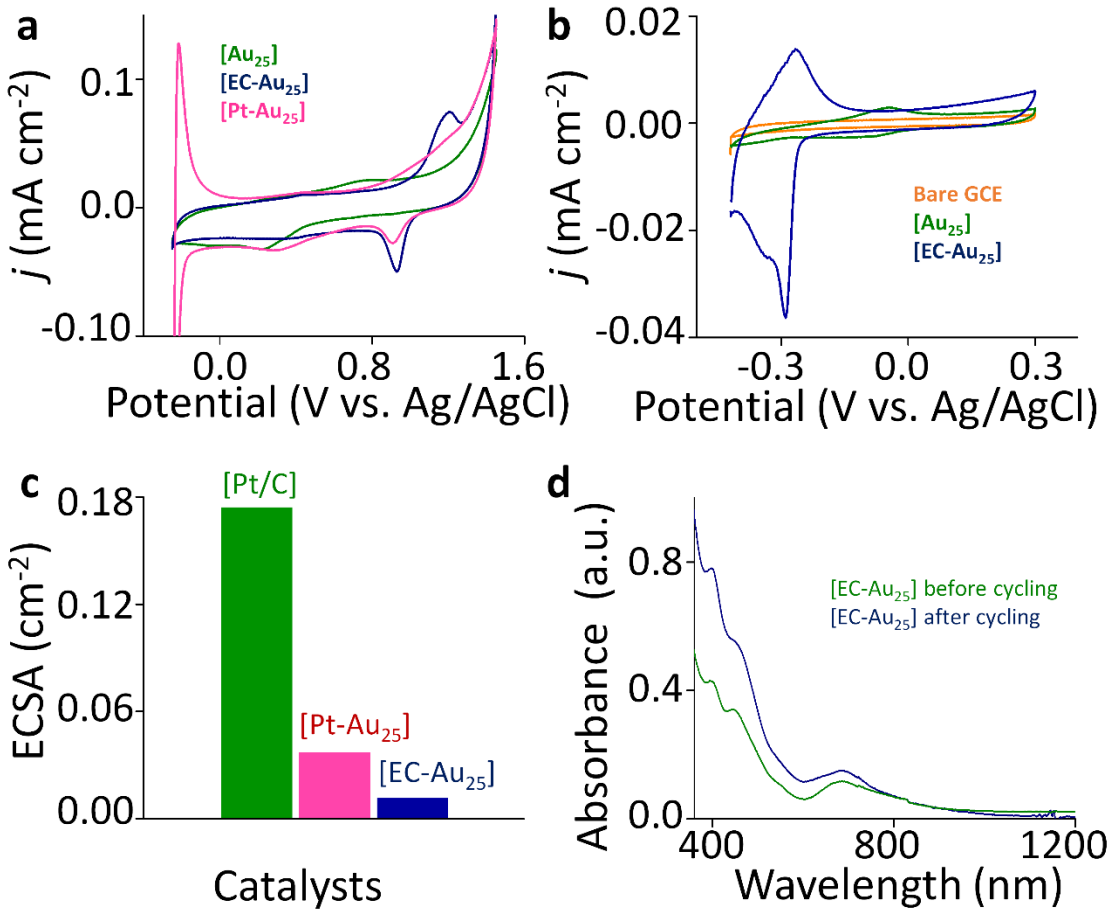

Figure 3: Electrochemical characterization of NCs. (a) cyclic voltammogram of Au_{25} (green), EC-Au_{25} (blue), and Pt-Au_{25} (pink) NCs in deaerated 0.1 M H_2SO_4 at 50 mV s^{-1}. (b) Cyclic voltammogram of Pb-UPD on Au_{25} and EC-Au_{25} with background curve at 20 mV s^{-1}. (c) ECSA of the Pt/C, EC-Au_{25}, and Pt-Au_{25} NCs. (d) UV-Vis absorption spectra of EC-Au_{25} NCs before and after Pb-UPD cycling.

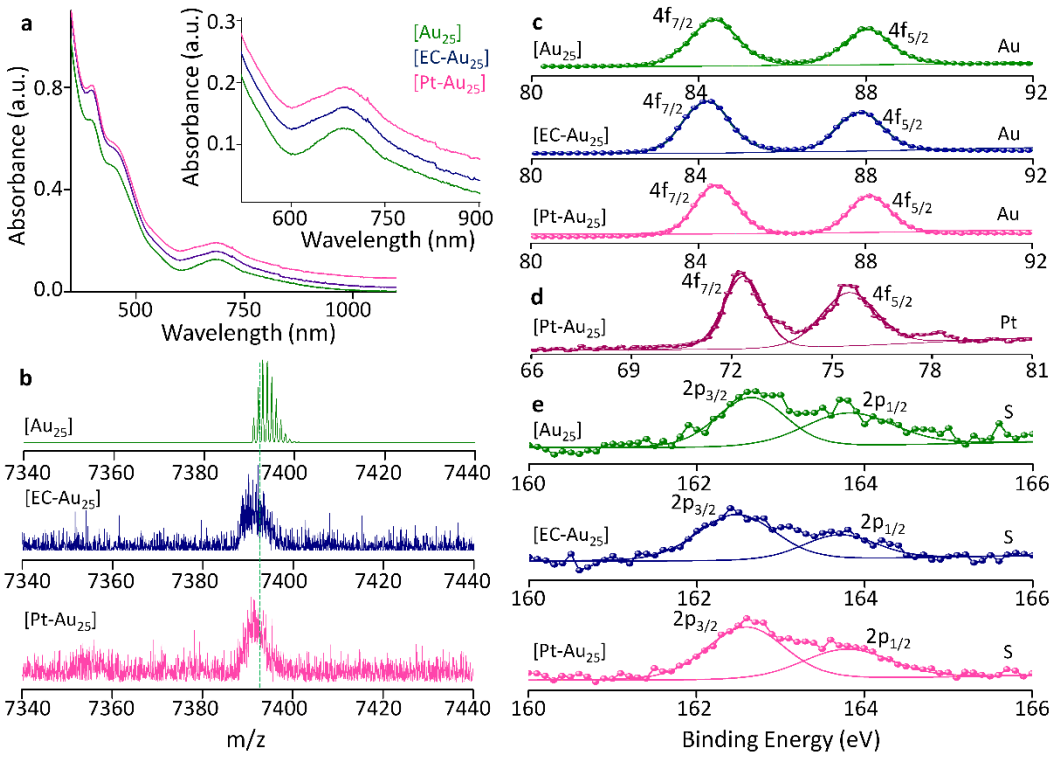

Figure 4: Spectroscopic characterization of Au_{25}, EC-Au_{25}, and Pt-Au_{25} NCs. (a) UV-Vis absorption spectra of Au_{25}, EC-Au_{25}, and Pt-Au_{25} NCs with the highlighted HOMO-LUMO region. (b) ESI-MS of Au_{25}, EC-Au_{25}, and Pt-Au_{25} NCs. XPS spectra of (c) Au 4f and (E) S 2p of Au_{25}, EC-Au_{25}, and Pt-Au_{25} NCs. (d) Pt 4f spectrum of Pt-Au_{25} NCs.

To further confirm the catalytic enhancement of EC-Au_{25} and Pt-Au_{25} NCs, their charge-transfer resistance (R_{ct}) was obtained using Electrochemical Impedance Spectroscopy (EIS) at an overpotential of 0.30 V vs Ag/AgCl. The Nyquist plots of Au_{25}, EC-Au_{25}, and Pt-Au_{25} NCs are shown in **Figure 5**f, in which the Randles equivalent circuit was used for fitting the experimental data (inset in **Figure 5**f). In the Nyquist plot, Pt-Au_{25} NCs showed the smallest semicircle (inset in **Figure 5**f) with an R_{ct} value of 549.3 Ω compared to EC-Au_{25} NCs (642 kΩ) corroborating well with the higher j_0 for Pt-Au_{25} NCs. The enhanced kinetics during the electrocatalytic HER is attributed to the exposed Au sites after the EC-activation of Au_{25} NCs. Further, EIS of Au_{25}, EC-Au_{25}, and Pt-Au_{25} NCs at different overpotentials (0.200, 0.250, 0.300,

0.350, 0.400, and 0.450 V vs Ag/AgCl) were performed to evaluate the dependency of potentials on R_{ct} (**Figure S15**a, b, and d). The R_{ct} values of all catalysts were decreased with increasing the applied overpotential, in accordance with the increased driving force. The EIS of all catalysts measured at open circuit voltage (OCV) is shown in **Figure S15**c. Nyquist plot of Pt-Au_{25} NCs (inset in **Figure S15**c) showed lower R_{ct} compared to Au_{25} and EC-Au_{25} NCs confirming their higher catalytic activity. In the Nyquist plot of Pt-Au_{25} NCs at an overpotential of 0.30 V vs Ag/AgCl and at OCV (**Figure S15**e), the R_{ct} value corresponding to OCV is found to be 100 Ω lower than that of 0.30 $V_{Ag/AgCl}$ applied potential. From the above data, it is clear that the catalytic activity of Pt-Au_{25} NCs is slightly inferior to Pt/C but highly superior to pristine Au_{25} NCs. Compared to EC-Au_{25}, the Pt-Au_{25} NCs showed the lowest overpotential of 0.117 V at 10 mA $cm^{-2}{}_{ECSA}$, the lowest Tafel slope of 86 mV dec^{-1}, and the smallest R_{ct} of 549.3 Ω indicating the highest HER kinetics and catalytic efficiency with ultralow loading of Pt. Another important factor is the long-term stability of the catalysts. To understand the stability of EC-Au_{25} and Pt-Au_{25} NCs, chronoamperometric measurements were conducted at a potential of -0.70 and -0.45 V vs Ag/AgCl, respectively, for 12 h. As shown in **Figure S16**a, Pt-Au_{25} NCs exhibited a steady current density response. However, in the case of the EC-Au_{25} NCs, the current density was increased with time, possibly due to the exposition of sites blocked by organic debris after EC-activation during HER. In contrast to the trend observed at low current densities, the commercial Pt/C and Pt-Au_{25} NCs exhibit lower reactivity at a higher current density (100 mA $cm^{-2)}$ than that of the EC-Au_{25} NCs (**Figure S16**b), although it has the lowest ECSA (**Figure 3**c). This might be a result of bubble nucleation and growth and their release.

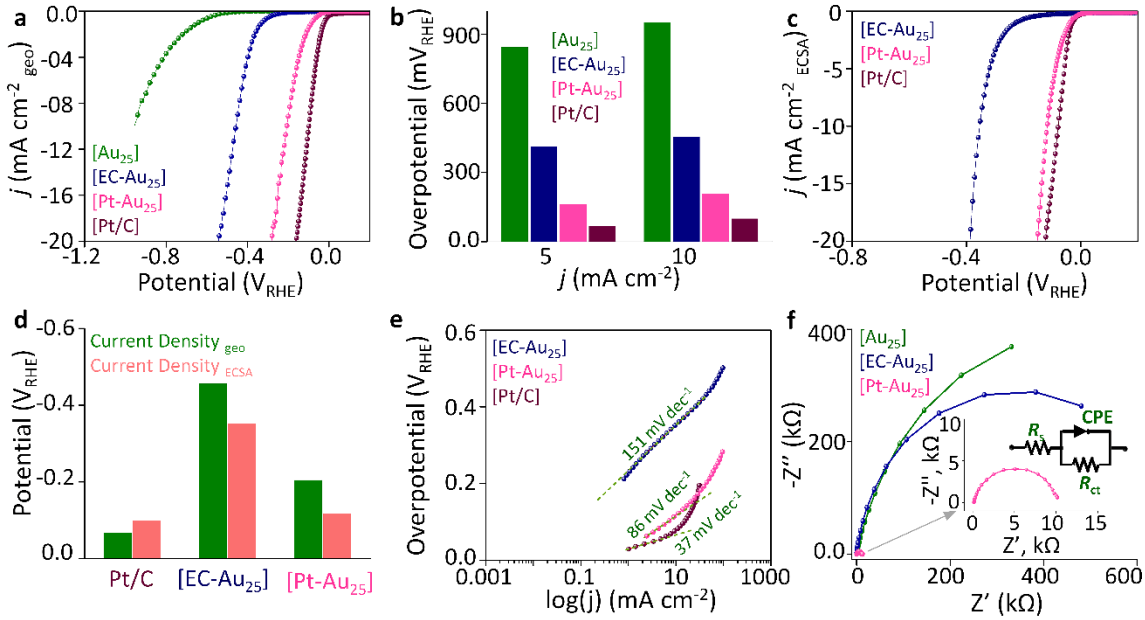

Figure 5: Electrocatalytic performances. (a) *iR*-corrected, geometric area normalized HER polarization curves of the Pt/C, Au_{25}, EC-Au_{25}, and Pt-Au_{25} NCs in 0.1 M H_2SO_4 at 5 mV s^{-1}. (b) Comparison of overpotentials at 5 and 10 mA cm^{-2} of Pt/C, Au_{25}, EC-Au_{25}, and Pt-Au_{25} NCs. (c) *iR*-corrected, ECSA normalized HER polarization curves of Pt/C, EC-Au_{25}, and Pt-Au_{25} NCs. (d) A comparison of overpotentials at 10 mA cm^{-2} with respect to geometrical area and ECSA of Pt/C, EC-Au_{25}, and Pt-Au_{25} NCs. (e) *iR*-corrected Tafel plots of Pt/C, EC-Au_{25}, and Pt-Au_{25} NCs. (f) EIS Nyquist plots for Au_{25}, EC-Au_{25}, and Pt-Au_{25} NCs (Inset: EIS of Pt-Au_{25} NCs).

In general, larger bubbles and higher bubble coverage at the surface could obstruct the active sites. Moreover, the electrically insulating bubbles would tend to reduce the available active sites and thereby increase the resistivity.[33] Rapidly releasing bubbles produced at a high reaction rate is crucial for ensuring: (i) the mechanical stability of the catalysts, (ii) the continuous exposure of the active sites, (iii) the efficiency of charge transfer kinetics, and (iv) the optimization of mass transfer efficiencies.[33b] The smooth *j-E* characteristics of EC-Au_{25} NCs even at 100 mA cm^{-2} presumably arise due to the easy removal of the bubbles at the reaction sites, which eventually facilitates the HER kinetics at higher overpotentials. Based on

these observations, a modified Volmer-Heyrovsky mechanism (as observed in thiolated Au NPs) is proposed, in which the adsorbed molecular hydrogen is initially formed in the Heyrovesky step [Eq. (1) and (3)].[8b] The subsequent slow desorption [Eq. (4)] of hydrogen would facilitate the formation of many smaller bubbles at the NC surface without any coalescence and formation of larger bubbles. On the other hand, Pt-Au_{25} NCs follow the Volmer-Tafel mechanism [Eq. (1) and (2)], where no adsorbed hydrogen molecule is expected, might result in faster formation and coalescence of bubbles leading the larger bubbles. The Pt catalyst follow the Volmer-Tafel mechanism, even on the sub-nanometer Pt clusters.[8c]

$Au + H^+ + e^- \rightarrow Au - H$	Volmer step	(1)
$2\,Au - H \rightarrow H_2$	Tafel step	(2)
$Au - H + H^+ + e^- \rightarrow Au - H_2$	Heyrovsky step (modified)	(3)
$Au - H_2 \rightleftharpoons Au + H_2$	Hydrogen desorption step	(4)

Scheme S2 illustrates the impact of lateral gas bubble accumulation, resulting in the formation of gaseous interphase that subsequently affects the reactivity of EC-Au_{25} and Pt-Au_{25} NCs. It is important to note that PEM electrolyzers are carried out in flow conditions and higher pressures (10-30 bar), where the bubble removal from the reaction site is easier. This implies that the Pt-Au_{25} NCs catalyst would exhibit higher current density at lower overpotentials. Providing the ease of bubble removal as in the case of EC-Au_{25} NCs under quiescent conditions, we assume that the reactivity would be still comparable with the Pt-Au_{25} NCs at higher current densities. The overall HER activity of Au_{25}, EC-Au_{25}, Pt-Au_{25}, and Pt/C are summarized in **Table 1**.

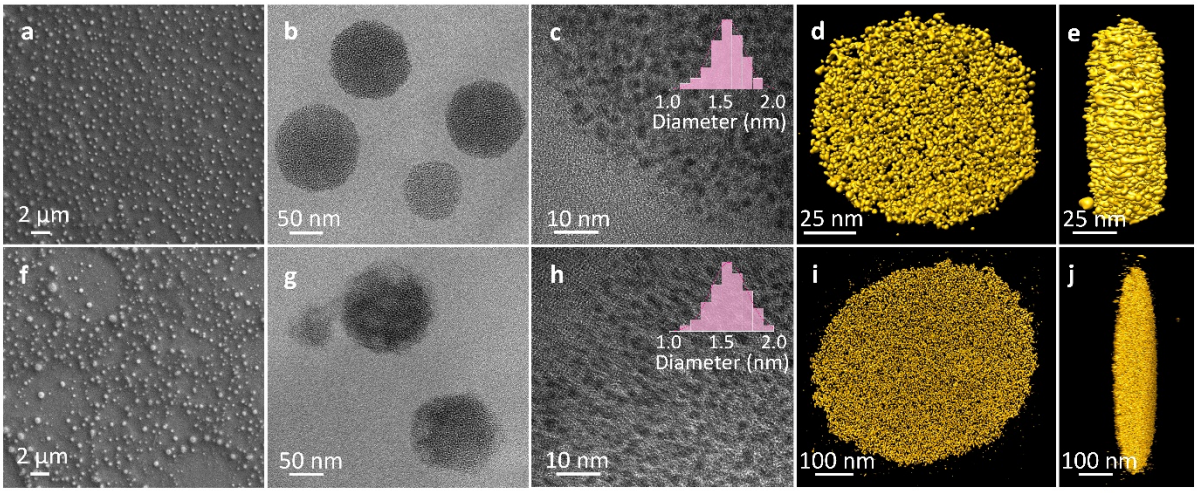

Figure 6: Morphology of EC-Au_{25}, and Pt-Au_{25} NCs. (a,f) FE-SEM images of EC-Au_{25}, and Pt-Au_{25} NCs. (b, g) HR-TEM images of self-assembled superstructures of EC-Au_{25}, and Pt-Au_{25} NCs and (c, h) corresponding higher magnification images with size distributions. Electron tomograms of self-assembled superstructures of (d, e) EC-Au_{25} NCs and (i, j) Pt-Au_{25} NCs projected in different orientations.

After EC-activation and Pt grafting, the morphology of NCs was studied using Field-Emission Scanning Electron Microscopy (FE-SEM). The FE-SEM micrographs (**Figures 6** a and f) show self-assembled superstructures of EC-Au_{25} and Pt-Au_{25} NCs (**Figure S17**a-d for higher magnification images). TEM images of EC-Au_{25} and Pt-Au_{25} NCs also found to be in good agreement with FE-SEM (**Figure 6** b and g). The HR-TEM images suggest that the size of NCs is still intact even after the EC-activation and Pt-grafting (**Figure 6** c and h). The formation of self-assembled structures of EC-Au_{25} NCs is presumably due to possible metallophilic interactions between the neighboring NCs due to partial dethiolation. A similar type of assembly is also seen in the case of Pt-Au_{25} NCs. In both cases, the TEM images show a nearly uniform size distribution of NCs (1.5 ± 0.5 nm; inset of **Figure 6** c and h, **Figure S18**). The EC-Au_{25} NCs assembly showed uniform contrast and electron transparency. However, Pt-Au_{25} NCs assembly showed lower contrast and uneven electron transparency due to the lack of aurophilic interactions after Pt-grafting. This is in line with cyclic voltammetry data, where the

gold oxide reduction peak is suppressed after Pt-grafting (**Figure 3a**). Further, the EC-Au_{25} and Pt-Au_{25} NCs were examined through Energy-Dispersive X-ray Spectroscopic (EDS) elemental mapping (**Figure S19**a-h). Based on the atomic wt% of EC-Au_{25} and Pt-Au_{25} NCs the amount of Pt decorated is found to be very low compared to the amount of Au and the ratio is 0.06. The Gray level intensity profile from the EDS map of Pt of Pt-Au_{25} NCs suggests that the distribution of Pt spans across the entire circular self-assembly (**Figure S21**). We further analyzed the surface topography of these self-assembled NCs using Atomic Force Microscopy (AFM) imaging (**Figure S20**a and b). From the 3D view (amplitude) of EC-Au_{25} and Pt-Au_{25} NCs (**Figure S20**c and d) and corresponding line profiles (**Figure S20**e and f), the average thickness of the circular assemblies of EC-Au_{25} and Pt-Au_{25} NCs is measured to be 35 ± 5 nm and 30 ± 5 nm, respectively. To gain further insights into the assembly, TEM tomography (ET) was performed for EC-Au_{25} and Pt-Au_{25} NCs. **Figures 5**d and e; and **Figures 5**i and j show the ET-reconstructed tomogram of EC-Au_{25} and Pt-Au_{25} NCs in different orientations, respectively ((TEM and ET reconstruction movies of EC-Au_{25} (**Video S1, S2**) and Pt-Au_{25} NCs (**Video S3, S4**). The thickness of the assembly is 40 nm and 35 nm for EC-activated and Pt-decorated NCs as measured from the tomogram. The ET data are in good agreement with AFM data.

Catalyst	Overpotential at 10 mA $cm^{-2}_{geo.}$ [V]	Overpotential at 10 mA cm^{-2}_{ECSA} [V]	Tafel [mV dec^{-1}]	ECSA [cm^2]	R_{ct} [Ω]	j_0 [mA cm^{-2}]
Au_{25}	0.956	-	-	-		-
EC-Au_{25}	0.456	0.353	151	0.0114	642x10^3	0.01
Pt-Au_{25}	0.205	0.117	86	0.0145	549.3	0.43
Pt/C	0.099	0.079	37	0.1747	-	0.18

Table 1. HER activities of the EC-Au_{25}, Pt-Au_{25} NCs, and Pt/C

3. Conclusion

In this work, we successfully demonstrated a facile and robust method for the preparation of highly active Pt-Au_{25} NCs using electrochemical activation enabled electroless-grafting of Pt

on $[Au_{25}(PET)_{18}]^-$ NCs. Grafting of Pt atoms is a self-termination process as it utilizes adsorbed hydrogen formed over exposed Au-sites upon dethiolation at -4 V for 1 s. Pt-Au_{25} NCs exhibited enhanced electrocatalytic activity towards HER with the overpotential of 0.117 V at 10 mA cm^{-2}, exchange current density of 0.43 mA cm^{-2}, and the Tafel slope of 86 mV dec^{-1}, even with ultra-low loading of Pt. Notably, this enhanced activity surpassed that of EC-Au_{25} NCs, which displayed an overpotential of 0.353 V, exchange current density of 0.01 mA cm^{-2}, and Tafel slope 151 mV dec^{-1}. The EC-Au_{25} and Pt-Au_{25} NCs exhibit remarkable stability over a twelve-hour period. The catalytic effect of Pt along with Au_{25} NC-mediated electron transfer is responsible for enhanced catalytic activity. Besides, EC-Au_{25} NCs possessed superior reactivity at high current density than Pt-Au_{25} NCs owing to the better bubble removal kinetics. The EC-activation uncovers unique supramolecular self-assembly characteristics of NCs enabled by metallophilic interactions. Our new strategy offers a wide opening for a variety of NCs in the area of electrocatalysis and robust hydrogen production to address the global energy and environmental crisis.

4. Experimental Section/Methods

Reagents and materials

All the chemicals and solvents are analytical grade and used without any further purification. gold(III) chloride trihydrate ($HAuCl_4 \cdot 3H_2O$), 2-phenylethanethiol (PET), tetraoctylammonium bromide (TOAB), sodium borohydride ($NaBH_4$), potassium hydroxide (KOH), potassium bicarbonate ($KHCO_3$), potassium chloride (KCl), sodium perchlorate ($NaClO_4$), perchloric acid ($HClO_4$), lead perchlorate ($Pb(ClO_4)_2$), sulfuric acid (H_2SO_4), methanol, acetone, tetrahydrofuran (THF), dichloromethane (DCM), acetonitrile, and toluene were purchased from Sigma-Aldrich. All the electrochemical measurements were performed using ultrapure water (Milli-Q, 18.2 MΩ cm resistivity).

Instrumentation and characterization

UV-vis absorption spectra were recorded using a VARIAN Cary 500 Scan spectrometer. High-Resolution-Transmission Electron Microscopy (HR-TEM) images, along with Scanning Transmission Electron Microscopic images, Energy Dispersive X-ray Spectroscopy (EDS) and elemental mapping were obtained utilizing an FEI Talos F200S transmission electron microscope operating at 200 kV. Field-Emission-Scanning Electron Microscopic (FE-SEM) images and EDS elemental profile were acquired employing a Carl-Zeiss SUPRA 55VP microscope. AFM images were acquired using an Agilent Technologies 5500 series AFM/SPM microscope equipped with Pico View 1.14.1 software, and the images were processed using WSxM 5.0. XPS spectra were collected using a Thermo Scientific ESCALAB 250Xi instrument with an XR6 Micro-focused Monochromator, utilizing AlKα X-rays. Electrospray Ionization-Mass Spectrometric (ESI-MS, Negative ion mode) measurements were performed using a Waters Synapt G2-Si high-definition mass spectrometer. GC-MS analysis was conducted using an Agilent 7890a GC and a 5975c Mass GC-MS spectrometer, equipped with a 30 m × 250 μm × 0.25 μm column. High-purity Helium served as the carrier gas, flowing at a rate of 1.0 mL min^{-1} with a split ratio of 10:1. Injections of 1 μL were carried out at 275 °C. The GC oven temperature was initially set at 70 °C and held for 2 minutes, followed by a ramp at 15 °C min^{-1} to 200 °C, where it was held for 5 minutes. A subsequent ramp at 20 °C min^{-1} elevated the temperature to 290 °C, which was maintained for the remainder of the 13-minute data collection period. MassHunter software was employed for data analysis. All electrochemical experiments were executed using a SP-200 BioLogic workstation.

Synthesis of $[Au_{25}(PET)_{18}]^-$ NCs

Au_{25} NCs were synthesized using a previously established procedure. In a solution containing $HAuCl_4 \cdot 3H_2O$ (20 mg/2 mL THF), TOAB (33 mg/1.75 mL THF) was introduced and stirred at 400 rpm for 15 minutes at room temperature. The initial yellow color of the solution

underwent a transformation to deep red during the stirring process. Following this, PET (34 µL; 5 mol equivalents relative to gold) was gradually introduced while maintaining the same stirring rate. The deep red shade gradually transitioned from red to yellow and eventually became colorless after roughly 1 hour of stirring. The resultant Au-thiolate solution was then subject to further reduction by injecting a freshly prepared ice-cold aqueous $NaBH_4$ solution (19 mg/1.25 mL; 10 mol equivalents relative to gold). This resulted in an instantaneous black coloration of the solution, which was then continuously stirred for an additional 8-9 hours. Upon the completion of the reaction, separation of the organic and aqueous phases was carried out using a separating funnel (augmented with 2 mL of toluene for enhanced partitioning). The organic layer was subsequently subjected to multiple washes with Millipore water to eliminate excess thiol and other impurities. The excess thiol and impurities were further removed by precipitating the NCs with the addition of 4 mL of methanol. This washing procedure was repeated three times. To eliminate insoluble Au-S polymers from the crude mixture, the NCs were extracted using DCM (dichloromethane). Ultimately, the NCs were re-suspended in acetone to eliminate byproducts (resulting in Au_{144} NCs). The dried Au_{25} NCs were preserved at 4 °C for subsequent characterization purposes.

Electrochemical Measurements

The electrochemical experiments were conducted using a two-electrode and three-electrode configuration and a biologic electrochemical workstation. Before utilization, the 3 mm diameter glassy carbon (GC) electrode underwent initial cleansing through polishing with 0.05 µm alumina powder, followed by a wash and 5-minute sonication in Milli-Q water. Post-cleansing, the GC electrode was modified by depositing 2 µL of synthesized Au_{25} NCs (obtained from 1 mg of NCs dissolved in 500 µL of dimethyl formamide) via drop-casting. The electrode was subsequently left to air-dry for 2 hours at room temperature. The EC-activation was performed with two electrodes where the GC electrode drop-cast with Au_{25} NCs

functioned as the cathode and a graphite rod (5 mm dia) as anode. For the HER studies, the NC-coated GC electrode acted as a working electrode with an Ag/AgCl (3 M KCl) electrode and Pt wire serving as the reference and counter electrodes, respectively. The HER performance of NCs was assessed using linear sweep voltammetry (LSV). The LSV measurements for the HER were conducted in a deaerated 0.1 M H_2SO_4 solution. The scan rate for these measurements was set at 5 mV/s, and the potential window ranged from 0.2 to -1.2 V *vs* Ag/AgCl at room temperature. The Pt/C catalyst ink was prepared by ultrasonication dispersing 1 mg of Pt/C 20 wt% in 750 µL of H_2O; 200 µL isopropyl alcohol; 50 µL Nafion 5 wt% solution. After 1 h, a homogeneous solution ink was obtained. The GC surface was modified by coating 2 µL of the Pt/C ink.

All potentials reported in this study have been calibrated with respect to the reversible hydrogen electrode (RHE), and all the CV and LSV were recorded with 85% of *iR* compensation.

Electrochemical activation and Pt decoration of Au_{25} NCs

The process of dethiolating Au_{25} NCs was carried out through an electrochemical (EC) activation approach. A glassy carbon electrode was employed as the cathode, where Au_{25} NCs were uniformly deposited (2.64 µg of gold) *via* drop-casting. Through chronoamperometry, EC activation was performed at a potential of -4 V for a duration of 1 s. Following this, the Au_{25} NCs on the glassy carbon electrode (EC-Au_{25} NC) were meticulously rinsed with ultrapure water to eliminate left-over salts and subsequently treated with methanol to remove the detached thiol molecules.

Next, the Pt decoration process on the dethiolated EC-Au_{25} NCs was conducted by immersing the electrode in a 1 µM solution of chloroplatinic acid at room temperature for 5 minutes. This step led to the formation of Pt-Au_{25} NCs on the electrode surface. The resulting Pt-Au_{25} NCs material was extensively washed with ultrapure water to eliminate any excess chloroplatinic acid.

The dethiolated EC-Au_{25} and the Pt-decorated Pt-Au_{25} NCs were subsequently utilized for conducting analysis of HER.

Pb-UPD measurements

The Pb-UPD experiment involved conducting cyclic voltammetry within a deaerated solution comprising a mixture of 0.1 M $NaClO_4$ and 0.01 M $HClO_4$ with 1 mM $Pb(ClO4)_2$ solution. A constant potential of -0.42 V was maintained for 60 seconds to facilitate under-potential deposition. Subsequently, the cyclic voltammetric curve was recorded from -0.42 to +0.3 V *vs* Ag/AgCl at a scan rate of 20 mV s^{-1}. Prior to the measurements, the electrolytes underwent de-aeration by subjecting them to N_2 bubbling for a duration of 20 minutes. The traces of oxygen in the nitrogen was scavenged by passing the nitrogen through alkaline pyrogallol scrubber before purging in the electrochemical cell.

EIS Measurements

EIS measurement was performed at open-circuit potential and at different overpotentials using conventional three-component electrode systems. The sinusoidal potential with the amplitude of 5 mV was superimposed over the ocp or dc-potential with the frequency range of 100 kHz to 1 mHz and at 10 points per decade. The in-buit Z-fit software in BioLogic SP-200 potentiostat was used for fitting the Nyquist plot.

Calibration of Ag/AgCl reference electrode to RHE

The potential was measured against Ag/AgCl reference electrode and corrected to RHE scale by measuring RHE potential. The RHE potential is measured using a Pt rotating disc electrode (RDE) at 900 rpm in 0.1 M H_2SO_4 by purging high-purity hydrogen for 30 minutes.

Gas Chromatography-Mass Spectrometry (GC-MS) experiments

Preparation of standard solutions for GC-MS calibration: Fresh stock solution of the PET (0.1 mM) was prepared in 10 mL of acetonitrile. Aliquots of this stock solution were mixed in the predefined molar ratios to yield a total of 500, 1000, 1500, and 2000 ng of PET in 1 mL of

acetonitrile. The thiol samples with unknown concentrations were prepared by washing Au_{25} NCs/GCE after EC-activation with fresh water to remove salts and then washed to 1 mL of acetonitrile to remove the detached thiols. The experiment was repeated 20 times with a total NC amount of 80 μg (20 x 4 μg = 80 μg). The samples were then analyzed on an Agilent 7890a GC and 5975c Mass GC-MS spectrometer.

The quantification of the removed thiol was calculated using a standard linear calibration curve obtained from the peak area of standard solutions analysis. The calibration curve was constructed using the standard solutions and the linear correlation was observed (500-2000 ng mL^{-1} of PET with the equation, y = 22.854x –228.2) with the linear regression coefficient (R^2) of 0.9926. The amount of removed PET was 1250 ng mL^{-1}, which was calculated by comparing the experimental area from the GC-MS peak at the RT of 6.86 with the calibration curve.

Microscopic Studies

HR-TEM images were acquired by drop-cast and dried approximately 100 μM of $[Au_{25}(PET)_{18}]^-$ NC in DCM onto a copper grid with a carbon-supported film. Following EC-activation and Pt-decoration, the EC-Au_{25} and Pt-Au_{25} NCs were detached from the glassy carbon electrode (GCE) surface by dissolving them in DCM. They were then drop-cast onto a carbon-supported copper grid for HR-TEM and on silicon wafer substrate for FE-SEM, and AFM analysis.

Supporting Information

Supporting Information is available from the Wiley Online Library or from the author.
Text S1-S10, Figures S1-S21, Scheme S1-S2, and Table S1-S2 as described in the text (PDF)
Videos S1-S4 as described in the text (MOV)

Author Contributions

The project was conceived by C.J. and supervised by C.J. and E.S.S. Synthesis and characterization of the nanocluster was executed by P.M. and J.V.R. The electrochemical

experiments were performed and the manuscript was drafted by P.M. The manuscript was written through the contributions of P.M., N., E.S.S., and C.J. Electron tomography data acquisition and reconstruction were performed by N. All authors have given approval to the final version of the manuscript.

Acknowledgements

C.J. thanks the Department of Science & Technology for funding through the SHRI scheme (DST/TDT/SHRI-42/2021). E.S.S. thanks the Science and Engineering Research Board (SERB) for the Ramanujan Fellowship (SB/S2/RJN-005/2017) and the Startup Research grant (SRG/2022/586). P.M. thanks the Council of Scientific and Industrial Research (CSIR) for a Junior Research Fellowship. The authors thank the DST Unit of Nanoscience (DST-UNS) and Thematic Unit of Excellence (TUE), IIT Madras, for their support for the measurements of ESI-MS and DFT calculations. The authors thank the Central Instrumentation Facility (CIF), CSIR-CECRI, for Instrumentation support. We acknowledge the Academy of Finland for project funding (No. 352900), Photonics Research and Innovation (PREIN) flagship and Tampere Microscopy Centre for imaging facilities. CSIR-CECRI Ethics and Scientific Vigilance Committee Reference Number: CECRI/PESVC/Pubs/2023-124.

Received: ((will be filled in by the editorial staff))
Revised: ((will be filled in by the editorial staff))
Published online: ((will be filled in by the editorial staff))

References

[1] a) M. S. Dresselhaus, I. L. Thomas, **2001**, *414*; b) M. Z. Jacobson, W. G. Colella, D. M. Golden, *Science* **2005**, *308*, 1901-1905.

[2] a) J. A. Turner, *Science* **2004**, *305*, 972-974; b) J. K. Norskov, C. H. Christensen, *Science* **2006**, *312*, 1322-1323; c) H. Yin, S. Zhao, K. Zhao, A. Muqsit, H. Tang, L. Chang, H. Zhao, Y. Gao, Z. Tang, *Nat. Commun.* **2015**, *6*, 6430.

[3] a) C. C. L. McCrory, S. Jung, I. M. Ferrer, S. M. Chatman, J. C. Peters, T. F. Jaramillo, *J. Am. Chem. Soc.* **2015**, *137*, 4347-4357; b) J. Zhu, L. Hu, P. Zhao, L. Y. S. Lee, K.-Y. Wong, *Chem. Rev.* **2020**, *120*, 851-918.

[4] J. Kibsgaard, I. Chorkendorff, *Nat. Energy* **2019**, *4*, 430-433.

[5] a) C. G. Morales-Guio, L.-A. Stern, X. Hu, *Chem. Soc. Rev.* **2014**, *43*, 6555; b) X. Zou, Y. Zhang, *Chem. Soc. Rev.* **2015**, *44*, 5148-5180.

[6] a) N. Cheng, S. Stambula, D. Wang, M. N. Banis, J. Liu, A. Riese, B. Xiao, R. Li, T.-K. Sham, L.-M. Liu, G. A. Botton, X. Sun, *Nat. Commun.* **2016**, *7*, 13638; b) P. Tang, H. J. Lee, K. Hurlbutt, P.-Y. Huang, S.Narayanan, C. Wang, D. Gianolio, R. Arrigo, J. Chen, J. H. Warner, M. Pasta, *ACS Catal.* **2022**, *12*, 3173-3180.

[7] R. Subbaraman, D. Tripkovic, D. Strmcnik, K.-C. Chang, M. Uchimura, A. P. Paulikas, V. Stamenkovic, N. M. Markovic, *Science* **2011**, *334*, 1256-1260.

[8] a) S. Yamazoe, K. Koyasu, T. Tsukuda, *Acc. Chem. Res.* **2014**, *47*, 816-824; b) G. Li, R. Jin, *Acc. Chem. Res.* **2013**, *46*, 1749-1758; c) K. Kuge, K. Yamauchi, K. Sakai. *Dalton Trans*., **2023**,*52*, 583-597.

[9] a) D. C. Lim, B. Y. Seo, S. Nho, D. H. Kim, E. M. Hong, J. Y. Lee, S.-Y. Park, C.-L. Lee, Y. D. Kim, S. Cho, *Adv. Energy Mater.* **2015**, *5*, 1500393; b) M. A. Abbas, S. J. Yoon, H. Kim, J. Lee, P. V. Kamat, J. H. Bang, *ACS Appl. Mater. Interfaces* **2019**, *11*, 12492-12503.

[10] a) T.-W. Koh, A. M. Hiszpanski, M. Sezen, A. Naim, T. Galfsky, A. Trivedi, Y.-L. Loo, V. Menon, B. P. Rand, *Nanoscale* **2015**, *7*, 9140-9146; b) Y.-C. Chao, K.-P. Cheng, C.-Y. Lin, Y.-L. Chang, Y.-Y. Ko, T.-Y. Hou, C.-Y. Huang, W. H. Chang, C.-A. J. Lin, *Sci. Rep.* **2018**, *8*, 8860.

[11] a) A. Mathew, P. R. Sajanlal, T. Pradeep, *Angew. Chem. Int. Ed.* **2012**, *51*, 9596-9600; b) T.-H. Chen, W.-L. Tseng, *Small* **2012**, *8*, 1912-1919.

[12] a) R. Jin, C. Zeng, M. Zhou, Y. Chen, *Chem. Rev.* **2016**, *116*, 10346-10413; b)I.Chakraborty, T. Pradeep, *Chem. Rev.* **2017**, *117*, 8208-8271; c) R. Jin, *Nanoscale* **2015**, *7*, 1549-1565; d) H. Häkkinen, *Chem. Soc. Rev.* **2008**, *37*, 1847; e) G. Schmid, *Chem. Rev.* 92, **1992,** *92*, 1709-1727; f) R. L. Whetten, J. T. Khoury, M. M. Alvarez, S. Murthy, I. Vezmar, Z. L. Wang, P. W. Stephens, C. L. Cleveland, W. D. Luedtke, U. Landman, *Adv. Mater.* **1996**, *8*, 428-433; g) J. F. Parker, C. A. Fields-Zinna, R. W. Murray, *Acc. Chem. Res.* **2010**, *43*, 1289-1296; h) J. V. Rival, P. Mymoona, K. M. Lakshmi, Nonappa, T. Pradeep, E. S. Shibu, *Small* **2021**, *17*, 2005718; i) J. V. Rival, P. Mymoona, R. Vinoth, A. M. V. Mohan, E. S. Shibu, *ACS Appl. Mater. Interfaces* **2021**, *13*, 10583-10593; j) J. V. Rival, P. Mymoona, E. S. Shibu, *Nanomaterials for Sensing and Optoelectronic Applications*, Elsevier, **2022**, pp. 149-15199; k) K. M. Lakshmi, J. V. Rival, P. Sreeraj, S. R. Nambiar, C. Jeyabharathi, Nonappa, E. S. Shibu, *Small* **2023**, *19*, 2207119.

[13] a) M. Zhu, C. M. Aikens, F. J. Hollander, G. C. Schatz, R. Jin, *J. Am. Chem. Soc.* **2008**, *130*, 5883-5885; b) M. A. Tofanelli, C. J. Ackerson, *J. Am. Chem. Soc.* **2012**, *134*, 16937-16940.

[14] a) H. Qian, Y. Zhu, R. Jin, *ACS Nano* **2009**, *3*, 3795-3803; b) O. Lopez-Acevedo, H. Tsunoyama, T. Tsukuda, H. Häkkinen, C. M. Aikens, *J. Am. Chem. Soc.* **2010**, *132*, 8210-8218.

[15] Y. Li, G. Galli, F. Gygi, *ACS Nano* **2008**, *2*, 1896-1902.

[16] a) L. Sumner, N. A. Sakthivel, H. Schrock, K. Artyushkova, A. Dass, S. Chakraborty, *J. Phys. Chem. C* **2018**, *122*, 24809-24817; b) D. R. Kauffman, D. Alfonso, C. Matranga, H. Qian, R. Jin, *J. Am. Chem. Soc.* **2012**, *134*, 10237-10243; c) S. Li, A. V. Nagarajan, X. Du, Y. Li, Z. Liu, D. R. Kauffman, G. Mpourmpakis, R. Jin, *Angew Chem Int Ed* **2022**, *61*; d) H. Seong, V. Efremov, G. Park, H. Kim, J. S. Yoo, D. Lee, *Angew. Chem. Int. Ed.* **2021**, *60*, 14563-14570; e) S. Zhao, R. Jin, H. Abroshan, C. Zeng, H. Zhang, S. D. House, E. Gottlieb, H. J. Kim, J. C. Yang, R. Jin, *J. Am. Chem. Soc.* **2017**, *139*, 1077-1080; f) W. Chen, S. Chen, *Angew. Chem.* **2009**, *121*, 4450-4453.

[17] a) K. Kwak, W. Choi, Q. Tang, M. Kim, Y. Lee, D. Jiang, D. Lee, *Nat. Commun.* **2017**, *8*, 14723; b) W. Choi, G. Hu, K. Kwak, M. Kim, D. Jiang, J.-P. Choi, D. Lee, *ACS Appl. Mater. Interfaces* **2018**, *10*, 44645-44653; c) Y. Li, S. Li, A. V. Nagarajan, Z. Liu, S. Nevins, Y. Song, G. Mpourmpakis, R. Jin, *J. Am. Chem. Soc.* **2021**, *143*, 11102-11108; d) S. Li, D. Alfonso, A. V. Nagarajan, S. D. House, J. C. Yang, D. R. Kauffman, G. Mpourmpakis, R. Jin, *ACS Catal.* **2020**, *10*, 12011-12016; e) S. Li, A. V. Nagarajan, D. R. Alfonso, M. Sun, D. R. Kauffman, G. Mpourmpakis, R. Jin, *Angew. Chem. Int. Ed.* **2021**, *60*, 6351-6356.

[18] a) D. Eguchi, M. Sakamoto, T. Teranishi, *Chem. Sci.* **2018**, *9*, 261-265; b) S. Li, A. V. Nagarajan, Y. Li, D. R. Kauffman, G. Mpourmpakis, R. Jin, *Nanoscale* **2021**, *13*, 2333-2337; c) J. Wang, F. Xu, Z. Wang, S. Zang, T. C. W. Mak, *Angew. Chem. Int. Ed.* **2022**, *61*, DOI 10.1002/anie.202207492; d) Y. Sun, X. Liu, K. Xiao, Y. Zhu, M. Chen, *ACS Catal.* **2021**, *11*, 11551-11560.

[19] M. Brust, G. J. Gordillo, *J. Am. Chem. Soc.* **2012**, *134*, 3318-3321.

[20] C. Jeyabharathi, S. Senthil Kumar, G. V. M. Kiruthika, K. L. N. Phani, *Angew. Chem. Int. Ed.* **2010**, *49*, 2925-2928.

[21] S. Zhuang, D. Chen, L. Liao, Y. Zhao, N. Xia, W. Zhang, C. Wang, J. Yang, Z. Wu, *Angew. Chem. Int. Ed.* **2020**, *59*, 3073-3077.

[22] S. Zhao, R. Jin, Y. Song, H. Zhang, S. D. House, J. C. Yang, R. Jin, *Small* **2017**, *13*, 1701519.

[23] a) J. V. Rival, Nonappa, E. S. Shibu, *ACS Appl. Mater. Interfaces* **2020**, *12*, 14569-14577; b) M. Zhu, E. Lanni, N. Garg, M. E. Bier, R. Jin, *J. Am. Chem. Soc.* **2008**, *130*, 1138-1139.

[24] S. Cherevko, N. Kulyk, C.-H. Chung, *Electrochim. Acta* **2012**, *69*, 190-196.

[25] Y. Li, Y. Jiang, M. Chen, H. Liao, R. Huang, Z. Zhou, N. Tian, S. Chen, S. Sun, *Chem. Commun.* **2012**, *48*, 9531-9533.

[26] a) A. Henglein, *Ber. Bunsenges. phys. Chem.* **1990**, *94*, 600–603; b) W. J. Plietht, *J. Phys. Chem.* **1982,** *86*, 3166-3170.

[27] a) C. Jeyabharathi, M. Zander, F. Scholz, *J. Electroanal. Chem.* **2018**, *819*, 159-162; b) A. Hamelin, *J. Electroanal. Chem.* **1984**, *165*, 167-180; c) A. Hamelin, J. Lipkowski, *J. Electroanal. Chem.* **1984**, *171*, 317-330.

[28] D. Thal, H. Kahlert, J. Chinnaya, P. Ahrens, U. Hasse, *J. Solid State Electrochem.* **2018**, *22*, 1149-1154.

[29] H. Qian, D. Jiang, G. Li, C. Gayathri, A. Das, R. R. Gil, R. Jin, *J. Am. Chem. Soc.* **2012**, *134*, 16159-16162.

[30] O. López-Estrada, N. Mammen, L. Laverdure, M. M. Melander, H. Häkkinen, K. Honkala, *ACS Catal.* **2023**, *13*, 8997-9006.

[31] S. Chen, M. Li, S. Yu, S. Louisia, W. Chuang, M. Gao, C. Chen, J. Jin, M. B. Salmeron, P. Yang, *J. Chem. Phys.* **2021**, *155*, 051101.

[32] S. Venkateshwaran, S. M. Senthil Kumar, *ACS Sustainable Chem. Eng.* **2019**, *7*, 2008-2017.

[33] a) W. Liu, X. Wang, F. Wang, K. Du, Z. Zhang, Y. Guo, H. Yin, D. Wang, *Na.t Commun.* **2021**, *12*, 6776; b) Y. Zhang, K. E. Arpino, Q. Yang, N. Kikugawa, D. A. Sokolov, C. W. Hicks, J. Liu, C. Felser, G. Li, *Nat. Commun.* **2022**, *13*, 7784.

Active platinum grafting Adsorbed hydrogen enabled electroless-grafting of Pt on $[Au_{25}(PET)_{18}]^-$ nanoclusters with minimal platinum loading scales the reactivity of hydrogen evolution reaction closer to benchmark Pt/C.

Paloli Mymoona, Jose V. Rival, Nonappa, Edakkattuparambil Sidharth Shibu, * *Chinnaiah Jeyabharathi* *

Platinum-Grafted Twenty-Five Atom Gold Nanoclusters for Robust Hydrogen Evolution